https://doi.org/10.3311/PPci.42128

Periodica Polytechnica Civil Engineering

Numerical Evaluation and Prediction of Bond Performance of Ribbed FRP and Steel Bars in Concrete Using Pull-out Test Simulations

Nizar Sadki[1*], Nasrine Belbachir[1], Sadek Bahar[1]

[1] Laboratory of Materials and Processes of Construction (LMPC), Department of Civil Engineering, Faculty of Science and Technology, Abdelhamid Ibn Badis University of Mostaganem, P. O. B. 188, National Road N11 Kharouba, 27000 Mostaganem, Algeria
[*] Corresponding author, e-mail: nizar.sadki@univ-mosta.dz

Received: 04 September 2025, Accepted: 21 February 2026, Published online: 16 March 2026

Abstract

This research investigates the bond behavior between concrete and ribbed reinforcement bars through numerical simulations of pull-out tests, focusing on three types of fiber-reinforced polymer (FRP) bars—Glass (GFRP), Aramid (AFRP), and Carbon (CFRP)—alongside conventional Steel bars, all with diameters ranging from 10 to 14 mm. Steel bars are modeled using a bilinear elastic–plastic constitutive law, while FRP bars follow a linear elastic behavior. The concrete modelled using a Regularized Coupled Damage–Plasticity Drucker–Prager Microplane approach. The interaction between concrete and reinforcement is simulated using a Mohr–Coulomb-type contact interface with friction coefficients tailored to each bar material, also accounting for mechanical interlock through explicit modeling of the rib geometry. The simulation results from the pull-out tests are compared against analytical bond–slip models and predictive formulations for maximum bond stress reported in the literature. Based on these comparisons, a new adapted predictive analytical model is proposed, showing improved agreement with the simulation data. The results indicate that CFRP bars exhibit in general the highest bond stress performance, followed by AFRP, steel, and GFRP. For all bar types, both the maximum bond stress and the corresponding slip decrease with increasing diameter. Steel bars exhibit higher and less predictable slip as a result of plastic deformation, whereas FRP bars demonstrate more stable and predictable behavior owing to their linear elastic response.

Keywords

simulation, friction, material, ribbed bars, bond-slip, pull-out, unconfined concrete

1 Introduction

In civil engineering, composite materials such as fiber reinforced polymer bars (FRP) are increasingly being used as substitutes for steel in reinforced concrete structures, especially in conditions where steel is exposed to corrosion [1]. Due to their enhanced resistance to corrosion and their lightweight nature, FRP bars constitute an attractive alternative to traditional steel bars [2, 3]. Furthermore, the programmable integration of mechanical properties and surface characteristics during manufacturing originates from their well-understood and stable constituent materials (fibers and polymer) [1]. This foundational stability, combined with the wider variety of contact surface configurations achievable in FRP bars compared to steel, enables targeted bond optimization and enhances the concrete reinforcement interaction [4]. This study investigates the bond performance between FRP bars and traditional steel bars in concrete, using numerical simulations of pull-out test as a key analytical method.

One of the major challenges to be addressed is to analyze the bond-slip behavior at the concrete-rebar interface through numerical simulation. In this context, discrepancies often arise between numerical results, experimental findings, and analytical models. However, in modern practice, these limitations can be mitigated due to advances in computing technology and the widespread availability of various structural simulation software [5].

Among these tools, ANSYS and ABAQUS are widely used for the numerical simulation of the bond behavior between concrete and rebars [5, 6]. In this study, ANSYS was selected not only for its ease of use but also for its robust capability to model the interactive behavior between two surfaces of different materials in a unified

Cite this article as: Sadki, N., Belbachir, N., Bahar, S. "Numerical Evaluation and Prediction of Bond Performance of Ribbed FRP and Steel Bars in Concrete Using Pull-out Test Simulations", Periodica Polytechnica Civil Engineering, 2026. https://doi.org/10.3311/PPci.42128

framework. Its advanced contact analysis features offer a reliable tool for simulating the interaction between concrete and rebar, making it possible to develop a simulation of the pull-out test that closely replicates experimental conditions [7, 8]. This numerical approach will significantly reduce the need for complex experimental campaigns, particularly in emerging countries where FRP bar technology remains both recent and less explored, and where limited access to sophisticated testing equipment presents a major challenge.

Several studies focus on numerical simulation of pull-out tests. Among these, Ibrahim et al. [9] conducted a numerical study on Basalt FRP (BFRP) bar–concrete bond mechanisms using finite element method (FEM) in ANSYS. The concrete was modelled with Hognestad's nonlinear compressive law and the ACI tensile model, alongside shear transfer coefficients. The bar–concrete interface was simulated using spring elements calibrated against an experimental pull-out data with Bilinear with Plateau and Exponential decay (BPE) bond–slip model. However, the BFRP bars were represented as linear elastic materials using smooth circular cross section bar without ribs geometry. In the study of Orlando and Benvenuti [10], a 3D regularized eXtended FEM (XFEM) approach was developed to simulate the steel/FRP–concrete interface behavior. The model incorporates a Rankine-type elastic damage law for concrete. The bar–concrete interaction neglects rib effects by representing both smooth and deformed bars as idealized smooth profiles, with calibrated damage parameters. Fava et al. [11] in their paper investigation on the bond of GFRP rebars and concrete, simulated pull-out tests in which bars were modeled as linear elastic and transversely isotropic, with a simplified smooth geometry without ribs geometry. Concrete was modeled using a linear elastic constitutive law, and the interface is simulated using a bonded surface by Virtual Crack Closure Technique (VCCT) for crack propagation and debonding. Zanuy et al. [12], simulated a pull-out test using ANSYS by modeling concrete as a nonlinear behavior combined with Willam-Warnke failure criterion. The interface was modeled using surface-to-surface contact elements, with Mohr-Coulomb friction and progressive debonding, with implicit integration of rib effects through adjusted parameters (cohesion, elevated friction), leading to a simplified smooth bar. A more advanced model for concrete Damage Plasticity (CDP) model, was employed by Tabatabaei Mirhosseini et al. [13] in their 3D finite element study using ABAQUS to investigate bond–slip behavior in reinforced concrete. The contact was simulated using an elastoplastic ring contact element to replicate concrete degradation at the interface. The rebar was modeled as a smooth, ribless round bar, while the effect of the ribs was implicitly incorporated through the adoption of the CEB-FIP code for bond stress–slip law governing the reinforcement–concrete interaction. Zhao and Zhu [5] and Wei-ping [14] conducted two studies on the bond behavior between concrete and reinforcement using pull-out simulation test. They adopted a multilinear isotropic (MISO) model combined with the Willam-Warnke multiaxial failure criterion for concrete, also considering the mechanical interlock, and they simulated the bar's rib geometry with a simplified profile, describing its mechanical behavior with a bilinear elastoplastic model, and representing the steel-concrete interface as a Coulomb-type frictional contact. However, the bond behavior analysis was confined to a single rib, thereby limiting the study to a local scale. A distinct concrete modeling approach presented by Eddy et al. [15] using the 3D Rigid Body Spring Model (RBSM) incorporates a Voronoi-based random mesh to realistically simulate crack propagation in concrete. An interfacial transition zone (ITZ) near the reinforcement is included, while a simplified rib geometry was initially considered for rebar modeling to capture mechanical interlock effects. In a recent study by García Sánchez et al. [16] the bond strength was analyzed employing numerical pull-out simulations. Using a microplane concrete damage model and frictional interaction contact, they compared auxetic rebars with conventional rebars. Two additional studies by Jin et al. [17] and Jiang et al. [18] focus on mechanical interlock by modeling the rebar with realistic geometry based on actual bars. Both studies employed the Concrete Damage Plasticity (CDP) model [13] for concrete and neglected chemical adhesion; however, the effect of friction was considered only in the first study [17]. Unlike all previous studies that used a static simulation approach, Panteki et al. [19] employed a dynamic simulation using LS-DYNA. The model incorporated the Soil and Foam Failure model for concrete, calibrated with triaxial experimental data. A tiebreak contact simulated initial adhesion, followed by steel–concrete friction after separation. The geometry included an explicit 3D representation of the rebar ribs, with the Piecewise Linear Plasticity model for steel.

Considering all the pull-out test simulations discussed so far, we will adopt the optimal conditions to accurately mirror experimental test environments in our investigation. We will replicate the overall shape that best corresponds

to the actual test [9–14, 16–19], while integrating the most representative damage model for concrete behavior [13, 16–18] and modeling the rib geometry [5, 14–16, 19]. Furthermore, as the primary goal of this research is to assess the bond behavior of FRP bars in relation to steel bars, we will also incorporate all other significant pull-out test variables like the variation in mechanical properties of reinforcing bar materials with various diameters [20]. Also taking into consideration the level of confinement of the concrete, which is crucial in the situation of the ribbed bars [20, 21]. This encompasses replicating and analyzing the behavior of each material individually via numerical simulation, including the tensile test for the bars [20] and the uniaxial compression/tension test of the concrete [22].

2 Pull-out test framework

The pull-out test is used to evaluate the bond strength between reinforcement and concrete. Bond behavior is generally represented by a curve illustrating the relationship between bond stress and relative slip, measured during the extraction of the bar from the concrete until failure occurs as shown in Fig. 1 [23]. To develop a simulation that accurately reproduces the actual conditions of the test, it is essential to rigorously identify and analyze all the key parameters influencing bond behavior. These include the bonding mechanism between concrete and reinforcement, potential failure modes, the material models used for both concrete and FRP/Steel bars, as well as the boundary conditions and the loading applied during the test. This approach allows us to precisely identify all the parameters necessary for the simulation.

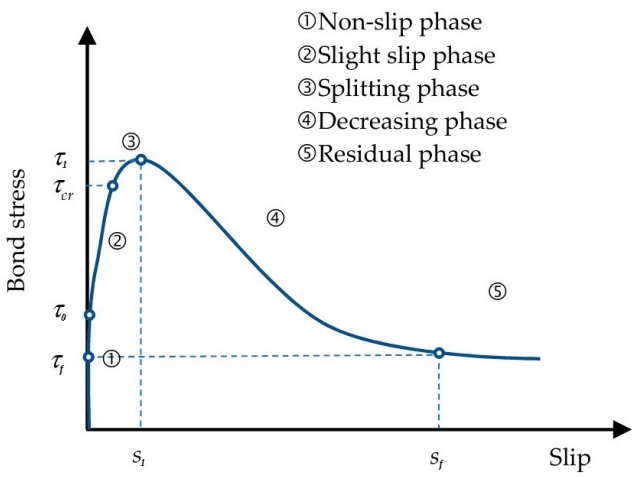

Fig. 1 Different phases of a typical local bond stress–slip curve between concrete and rebars [23]

2.1 Bond mechanisms

In this research, we investigate the bond behavior between concrete and ribbed reinforcing bars. It is therefore crucial to understand the bonding mechanisms in order to determine the parameters governing the interaction between the two materials under the key conditions of the pull-out test simulation.

2.1.1 Chemical adhesion

The chemical adhesion between the surface of the bar and the concrete occurs initially as the concrete sets. This bond is relatively weak and mainly helps in establishing initial adhesion. Generally, the chemical bonding of FRP bars tends to be relatively weak due to the characteristics of the chemical interaction between the concrete and the constituents of the FRP bars [1, 23]. In contrast, a perceptible chemical bond exists between steel and concrete due to the chemical reaction that takes place during setting, whether for ribbed or smooth bars [2]. The chemical bonding stress is less than 2 MPa [5, 24], a value that is very low compared to the bond of ribbed bars during the pull-out test [1, 25]. There is also the corrosion effect on steel bars, which can break the chemical bond between concrete and steel bars [1, 23]. Thus, we can conclude that the chemical bonding effect is too weak compared to the overall bonding performance of ribbed bars [26]. Thus, we choose to neglect the chemical bonding effect for steel bars, and by extension, for FRP bars, which exhibit a much weaker chemical bond.

2.1.2 Friction

When the pull-out force is applied, a resistance is generated due to the friction between the surface of the bar and the concrete. This resistance is influenced by both the texture of the bar interface and the roughness of the concrete surface. Moreover, the coarse surfaces of FRP bars might enhance friction at the contact point [5]. The quantity representing the friction between concrete and reinforcement is generally expressed by the friction coefficient (μ) [5, 12, 13]. To simulate this mechanism, we will use friction coefficient values that reflect the texture of each bar in interaction with the concrete. The friction coefficient between ribbed steel bars and concrete is typically equal to 0.4, according to the practical code CSTB [27]. However, several experimental studies and simulations indicate a more precise value, ranging from 0.26 to 0.28 [5, 28–30].

Regarding FRP bars, research on determining the friction coefficient for ribbed bars remains limited due to their

more recent use compared to steel and the broad range of surface conditions. Thus, to estimate the friction coefficients of FRP bars, we will focus on the interaction between FRP materials and the texture of the concrete [31], which is typically influenced by the aggregate size at the contact surface [32]. Additionally, we will take into account the friction of the components of the FRP, specifically the resin in contact with the concrete [33]. For GFRP composites, the friction coefficient with concrete is approximately 0.6 under optimal conditions [31]. The friction of FRP also varies depending on the roughness of the sand grains in the concrete [32]. For steel, the coefficient of friction is around 0.3, while for CFRP it ranges from 0.22 to 0.51 and for GFRP from 0.29 to 0.62 [32]. Furthermore, the friction between FRP and concrete also depends on the friction between the resin and concrete, which ranges from 0.46 for normal concrete to 0.65 [33]. Therefore, considering all the previous data, we propose an average friction coefficient value of 0.3 for steel [32]. For FRP, we suggest a friction coefficient of 0.4 for CFRP, slightly higher than steel's 0.3 [32]. For GFRP a value of 0.6 [31]. For AFRP we propose a friction coefficient of 0.5.

2.1.3 Mechanical interlock

The mechanical interlock occurs when the concrete conforms to the shape of the ribs during pouring. After the concrete hardens, it creates a lock around the ribs of the bars, preventing slip between the concrete and these ribbed bars. This mechanical interlock is essential for the overall bond strength [5]. This mechanism is represented in the simulation by modeling the geometric shape of the ribs [5]. Although very recent simulations interpret realistic rib shapes to study the form [17, 18], for our study, we will limit ourselves to conventional rebars model [5, 14–16, 19] for all bars, for two main reasons: first, our study focuses on observing the influence of material type variation rather than geometry ribs. Second reason, the choice of the quadratic CPT216 cubic finite elements, essential for the convergence of the concrete model used in our simulation [7], which makes it computationally incompatible with intricate rib geometries [17, 18].

2.1.4 Concrete confinement

Concrete confinement refers to the ability of the concrete surrounding the bar to resist the stresses induced by pull-out forces. This confinement is essential for maintaining and improving the bond strength between concrete and reinforcement bars. Adequate confinement—whether provided by transverse reinforcement, external pressure, or concrete cover thickness enables the concrete to sustain higher shear stresses and delay the formation and propagation of cracks under pull-out loading [34]. In this study, an unconfined concrete (UC) with a compressive strength class of 6000 psi, without any transverse reinforcement, is considered [22].

2.2 Failure modes

The main parameter governing the failure mode is the degree of confinement (K) of concrete [34] as illustrated in Fig. 2. There are four main failure modes commonly observed in reinforcement pull-out tests, which are crucial for accurate modeling and prediction of bond behavior:

- **Slip or Strip Failure:** Occurs in unconfined concrete, leading to bond degradation between ribbed bars and concrete and a progressive loss of resistance as slip increases.
- **Splitting Failure:** Typical for moderately confined concrete ($K < 6$). It results from tensile stresses causing radial cracks and longitudinal splitting.
- **Pull-out Failure:** Observed when bond strength is exceeded despite fully confinement ($K \geq 6$); the bar is pulled out along with shear failure of the concrete around the ribs.
- **Bar Rupture:** Occurs when the tensile strength of the reinforcement bar itself is surpassed before bond deterioration, typically in highly confined concrete or with long anchorage lengths.

In general, the common factors influencing failure modes are related to concrete behavior, including cracking under brittle response in tension and nonlinear behavior under compression, where crack propagation leads to

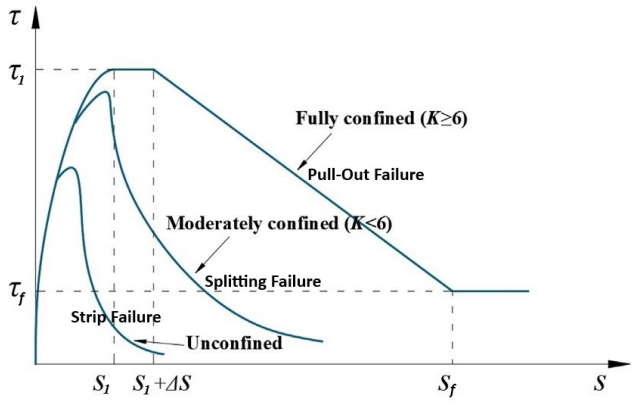

Fig. 2 Typical local bond stress–slip curves between concrete and rebars for different degrees of confinement [34]

a gradual reduction in load bearing capacity as the applied load increases. This underscores the need for appropriate numerical models that account for these effects to accurately simulate concrete [13, 16–18].

2.3 Concrete model

The concrete was modeled using a regularized coupled with damage plasticity (DP) Drucker-Prager (DP) Microplane (MP) model [35], designed to replicate its nonlinear response under axial loading. The elastic properties of the material, such as Young's modulus (E_c) and Poisson's ratio (v), define its stiffness and lateral deformation. The plasticity component incorporates a three-surface yield function (Fig. 3), combining the uniaxial compressive strength (f_{uc}), tensile strength (f_{ut}), and biaxial compressive strength (f_{bc}), along with a compression Drucker-Prager cap governed by the transition stress (σ_v^c) and a shape parameter (R_c), and a tension cap associated with a hardening factor (R_t) and a global hardening parameter (D). Damage is driven by critical thresholds in tension and compression (γ_{t0}, γ_{c0}) marking the initiation of cracking, as evolution parameters (β_t, β_c) regulate damage progression. To stabilize numerical results, nonlocal gradient regularization is applied via an over-nonlocal parameter (m) and an interaction range (c), linked to element size (L). This method mitigates numerical singularities by distributing damage across a physically representative area, aligning model predictions with the realistic propagation of cracks observed experimentally.

2.3.1 Material parameters for concrete simulation

To simulate concrete model in ANSYS, both elastic and plastic material parameters must be defined, as detailed in Table 1. In our case, we will incorporate all these plastic characteristics, along with the elastic parameters, using ANSYS Parametric Design Language (APDL) instructions [7]. In the simulation, we use Concrete Class 6000 psi, which is designed to achieve a minimum compressive strength of 6000 psi (approximately 41 MPa) defined as class C40, when tested at 28 days of curing. For the degree of confinement of concrete, we opted for an unconfined concrete model, denoted as UC (see Table 1), by proposing appropriate values for the hardening parameter (D) and the compression damage parameter (β_c) to model the behavior of unconfined concrete.

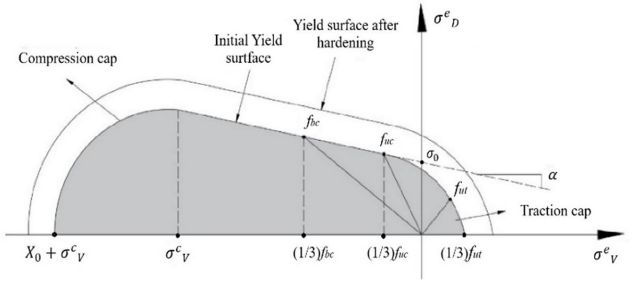

Fig. 3 Three-surface Drucker–Prager microplane smooth cap yield function

Table 1 Parameters for the concrete DP-DP-MP model for simulation

Behavior	Parameter	Formula	Units	UC
Elasticity	E_c	$4700\sqrt{f_{uc}}$	MPa	3E4
	v	$0.15 \leftrightarrow 0.25$	–	0.2
Plasticity (DP)	f_{uc}	Experimental	MPa	41
	f_{bc}	$1.15f_{uc}$	MPa	48
	f_{ut}	$0.1f_{bc}$	MPa	4.8
Hardening	R_t	1	–	1
	D	$10^4 \leftrightarrow 5 \times 10^5$	–	4×10^5
Compression cap	σ_v^c	$-(2/3)f_{bc}$	MPa	−32
	R_c	2	–	2
Damage	γ_{t0}	0	–	0
	γ_{c0}	$10^{-5} \leftrightarrow 10^{-4}$	–	5E-5
	β_c	$1000 \leftrightarrow 10000$	–	4000
	β_t	$(3/2)\beta_c$	–	6000
Nonlocal	c	$>4L^2$	mm^2	1600
	m	$1 \leftrightarrow 3$	–	1

2.3.2 Simulation of concrete under uniaxial tests

To set up a uniaxial test simulation in ANSYS, begin by defining the geometry of the test specimen, as 100 mm concrete cube, and specifying the material properties for the concrete model using APDL. In order to simulate accurately concrete in a plastic model, SOLID216 elements with a mesh size of 1 mm are adopted [7]. Next, apply the boundary conditions by fixing one end of the specimen and imposing a compare load through a gradually increasing displacement at the opposite end, ensuring a realistic simulation of the experimental conditions. To obtain the results of the uniaxial test in compression as well as in tension, the imposed displacement at the free end is specified as a negative value for the compression test (5 mm) and as a positive value for the tension (1 mm).

The simulation (Fig. 4) accurately reproduces the behavior of unconfined concrete. In compression, the curve shows a linear response up to about 32 MPa, followed by slight hardening, which reflects the absence of confinement, reaching a peak of 40.9 MPa (consistent with the 6000 psi class), and then gradually softening to failure. In tension,

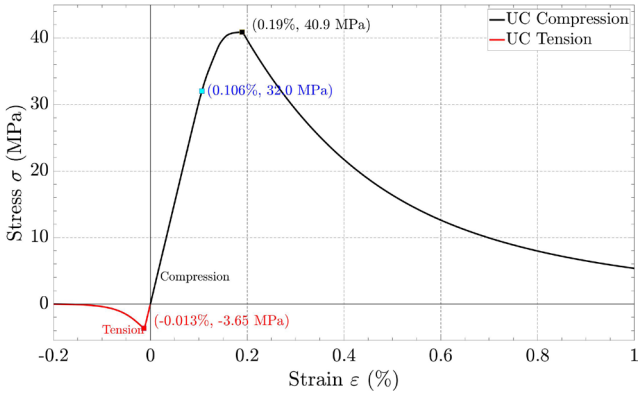

Fig. 4 Stress-strain curves for concrete from uniaxial tests simulation

the behavior is brittle, with a significantly lower strength of 3.6 MPa (less than 10% of the compressive strength) and sudden failure immediately after the peak. This highlights concrete's asymmetric strength response.

2.4 Rebars models

The mechanical behavior of conventional steel reinforcement bars under load generally exhibits two distinct phases: an elastic phase followed by a ductile response, allowing significant deformation before failure. This ductility is advantageous in concrete structures, as it enables energy dissipation and provides visible warning signs before ultimate failure. To simulate steel, the bilinear isotropic hardening material model is employed [9].

The initial segment represents the elastic response of the steel, defined by its modulus of elasticity and yield strength. The second segment captures the plastic behavior, characterized by a tangent modulus approximately 1% of the elastic modulus and a tensile strength corresponding to the ultimate strain, as detailed in Table 2 [24].

In contrast, FRP bars exhibit brittle behavior, as indicated by their linear stress–strain response up to failure. However, they offer higher tensile strength, lower density, and excellent corrosion resistance compared to conventional steel. Therefore, they are modeled as linear elastic materials, defined by their Young's modulus and ultimate tensile strength, as detailed in Table 2 [24].

Table 2 Parameters for the concrete DP-DP-MP model for simulation

Mechanical properties	Steel	GFRP	CFRP	AFRP
Yield stress (MPa)	400	NA	NA	NA
Tensile strength (MPa)	460	708	1860	1470
Elastic modulus (GPa)	200	46.3	127.5	75.8
Poisson's ratio	0.3	0.26	0.25	0.25
Yield strain (%)	0.2	NA	NA	NA
Rupture strain (%)	3	1.5	1.4	1.9

2.4.1 Simulation tensile test of rebars

To set up a uniaxial tension test simulation for rebars in ANSYS, start by defining the geometry of the rebar specimen, typically a cylindrical bar with a 14 mm diameter and a length of 100 mm, corresponding to the experimental setup, where the length varies between 25 mm and 100 mm. Assign the appropriate material properties, considering the elastic and plastic behavior of steel or FRP from Table 2. The load is applied by fixing one end of the rebar and imposing a displacement of 5 mm on the free end. The results of the uniaxial tensile test simulations for steel and FRP bars, as shown in Fig. 5, produced diagrams consistent with those presented in the codes of practice ACI Committee 440 [3]. This indicates that the numerical models employed accurately reflect the actual behavior of these materials, thereby validating the accuracy of the results against reference standards.

3 Pull-out test simulation model

The pull-out test simulation model is based on many experimental studies [11, 13, 24, 36–38], which use either a cubical or cylindrical geometry for the concrete block with a larger around 10 times the rebar diameter (d_b) [36]. Three typical configurations Models 1, 2 and 3 are illustrated in Fig. 6. Each includes a bonding zone (Zone A) with a height generally around 4 to 5 times the rebar diameter (d_b), corresponding to the embedment length (l_e). The proposed simulation model for zone A focuses specifically on this charred Zone A, as shown in Fig. 6. Due to the significant computation time required to solve this model in ANSYS, as well as the large number of simulations needed to complete this research, a simulation optimization approach was implemented to reduce the time without compromising the accuracy of the contact results between concrete and reinforcement. Thus, a reduced model for Zone B was proposed (Fig. 6), allowing for

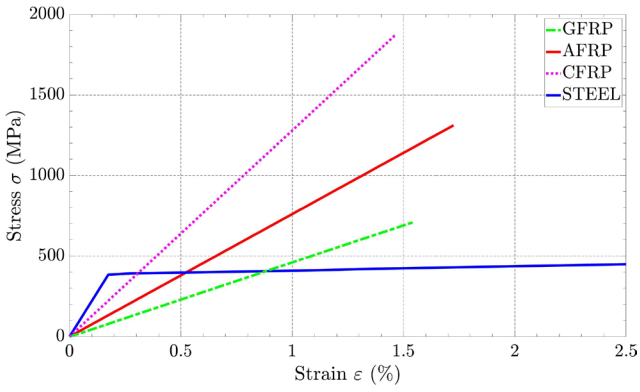

Fig. 5 Stress-strain curves for concrete from uniaxial tests simulation

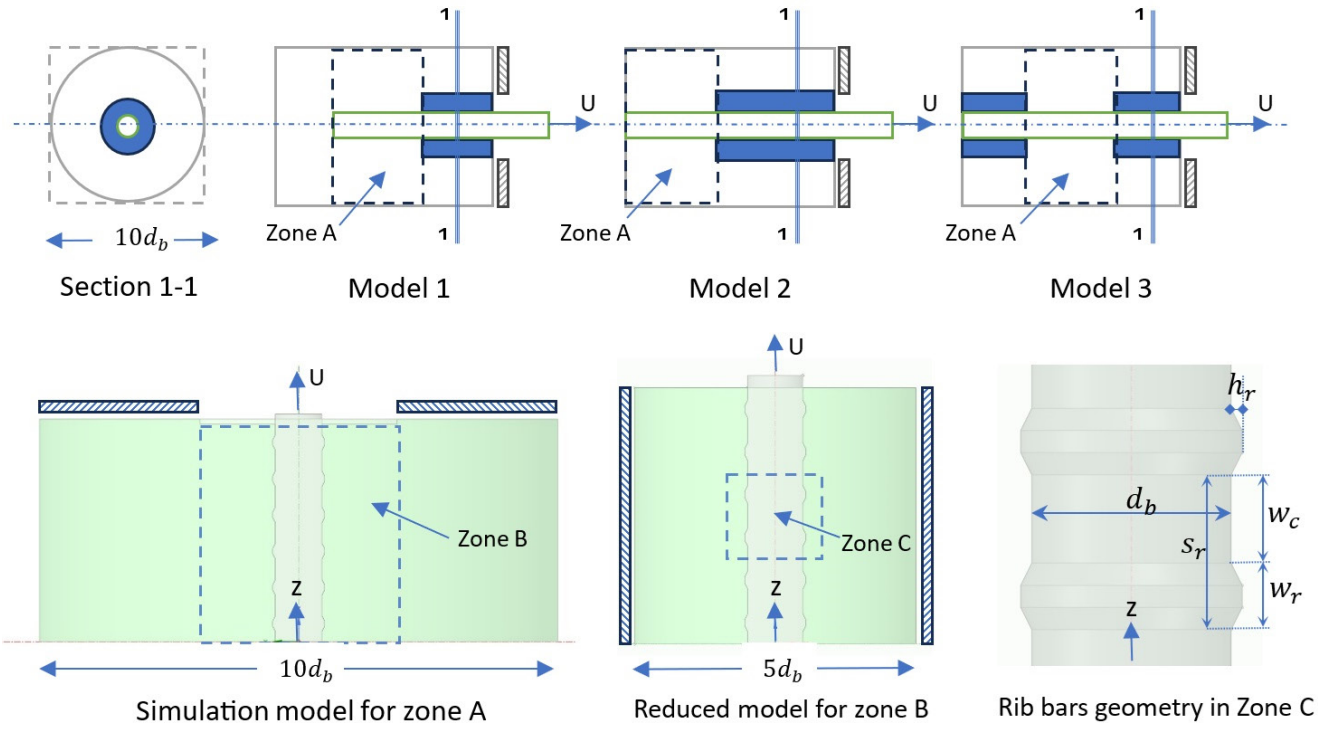

Fig. 6 Simulation model for the pull-out test

comparable results to the original models while decreasing solving time. This reduction is based on experimental evidence from tests [21, 23], showing that the concrete cover thickness should range between 2.5 and 3.5 times the reinforcement bar diameter.

Therefore, we adopted a value of $2.5d_b$ which corresponds to our cylindrical reduced model with a total width of $5d_b$ and a height corresponding to the embedment length (l_e) set to 50 mm. For the geometric characteristics of the bars, different diameters of 10 mm, 12 mm, and 14 mm were used, while the rib geometry of bars in Zone C (Fig. 6) remained unchanged, with a rib height h_r = 1 mm and width w_f = 3 mm, with a spacing of s_r = 8 mm. The concrete rib width was considered to be w_c = 8 mm.

The boundary conditions were defined as follows: the pull-out load on the reinforcement was simulated by applying an imposed displacement U ranging from 0 to 10 mm with an increment of 0.01 mm. The outer peripheral surface of the reduced cylindrical model was constrained, a condition commonly adopted in similar studies [37], which also mimics the effect of reduced concrete cover thickness.

The coefficient of friction depends on the reinforcement material, as explained earlier in the literature: 0.3 for steel, 0.4 for CFRP, 0.5 for AFRP, and 0.6 for GFRP bars. To represent the variation of the bond stress as a function of the bar slip, the bond stress corresponds to the reaction force at the level of the bar divided by the contact surface area between the concrete and the bar, extracted from simulation for each bar diameter. This force corresponds to the applied force on the bar in the experimental tests [24, 34, 38].

3.1 Simulation results

The results of the simulation are presented in Fig. 7 (a), showing the variation of the force as a function of slip. The force is provided by the reaction force tool due to the imposed displacement in ANSYS. The slip, on the other hand, is the mean displacement of the bar, extracted directly from the simulation for each modeled specimen.

The force variation begins at approximately 5 KN for all cases. This is followed by a linear plateau that reaches about half of the peak force. Then, the curve adopts a convex hyperbolic shape until it reaches the maximum value, followed by a descending hyperbolic branch. The maximum force values increase proportionally with the bar diameter. This can be explained by the fact that the resulting bond stresses—calculated by dividing the reaction forces by the contact surface area related to the diameter—are of more comparable magnitudes. It is noted that the slip values decrease as the diameter increases. For the bond stress versus slip curves Fig. 7 (b), their shape corresponds to that of the typical unconfined concrete behavior curve, as described in Fig. 2, corresponding to a strip failure mode characterized by progressive shear and crushing of concrete between the ribs. It can be observed that the response

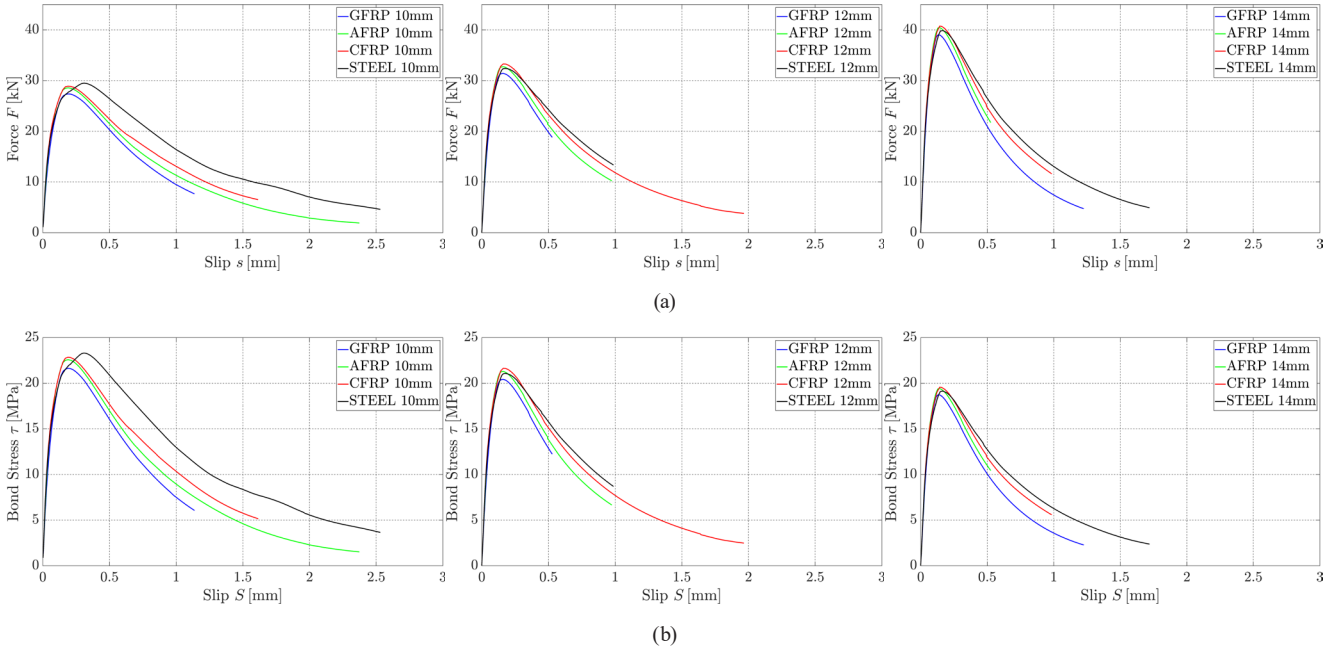

Fig. 7 (a) Reaction force–slip curves and (b) bond stress–slip curves from pull-out simulation results for d_b = 10 mm, d_b = 12 mm and d_b = 14 mm

follows the same stages as the typical local bond stress–slip curve described in Fig. 1, except for the fifth stage. This is because unconfined concrete exhibits negligible residual bond stress as shown in Fig. 2. Thus, our curves follow bond-slip model with four stages explained as follows:

- **Step 1:** At the initial loading phase, a short linear segment appears without slip, mainly due to the mechanical interlock and the static friction effect between the bar and the concrete, approximately $\tau_0/\tau_1 \approx 0.1$.
- **Step 2:** The bar begins to slip against the concrete, following a monotonically linear trend up to approximately $\tau_{cr}/\tau_1 \approx 0.5$. At this stage, the friction coefficient, combined with tangential stresses resulting from the mechanical interlocking of the ribs, resists the movement of the bar. This interaction increases the bond stress, producing a nearly straight curve shape, mainly due to the linear elastic behavior of the concrete under compression in the adopted model.
- **Step 3:** As the load continues to increase, the bond stress curve follows a parabolic shape up to the maximum stress τ_1 primarily due to the hardening behavior introduced in the concrete model used in the simulation, which experimentally corresponds to the crushing of the concrete caused by the penetration of the bar ribs into the concrete ribs, thereby simulating the shearing of concrete ribs and leading to strip failure.
- **Step 4:** Beyond the ultimate bond stress τ_1, the bond stress sharply decreases while the slip rapidly increases along a hyperbolic curve. This stage corresponds to the post-peak softening behavior of the concrete model, as the material between the ribs exceeds its strength and enters a damage-softening phase, thereby mimicking the real progressive degradation of bond strength.

3.2 Bond–slip curve shape validation

For the validation of the bond stress–slip diagrams, two analytical models assuming unconfined concrete, consistent with our simulation conditions. Model 1, proposed by Rolland et al. [38] shown in Fig. 8, was selected due to its demonstrated robustness across a wide range of bond tests involving steel and various FRP bars with different surface textures. Model 2, developed by Lu et al. [39] and illustrated in Fig. 8, was adopted based on its proven

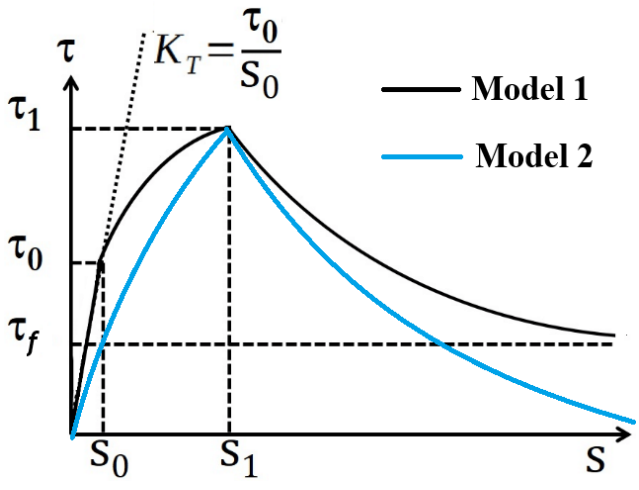

Fig. 8 Bond-slip model 1 by Rolland et al. [38], model 2 by Lu et al. [39]

reliability through validation against several established prediction models. The parameters of both models are calibrated using the numerical data obtained from the pull-out test simulation, as summarized in Table 3.

3.2.1 Analytical model 1

The bond-slip response associated with this model is shown in Fig. 8. It consists of a first linear ascending branch with finite slope $K_T = \tau_0/s_0$, followed, for slip values above s_0, by a non-linear (hyperbolic) branch reaching τ_1 when the slip is equal to s_1. Finally, it includes a third descending branch (also of hyperbolic type), with a horizontal asymptote tending to τ_f. The two parameters α and β govern the curvatures of the ascending and descending branches, respectively [38]. This model, expressed by relationship in Eq. (1), is governed by seven parameters: s_0, τ_0, s_1, τ_1, τ_f, α, β:

$$\tau(s) = \begin{cases} \tau_0 \dfrac{s}{s_0}, & 0 \le s \le s_0 \\ \tau_0 + (\tau_1 - \tau_0)\left(1 + \dfrac{1}{\alpha}\right)\left(1 - \dfrac{1}{1 + \alpha\left(\dfrac{s - s_0}{s_1 - s_0}\right)}\right), & s_0 < s \le s_1 \\ \tau_f + (\tau_1 - \tau_f)\left(\dfrac{1}{1 + \beta\left(\dfrac{s - s_1}{s_1}\right)}\right), & s_1 < s \le s_f \end{cases} . \quad (1)$$

3.2.2 Analytical model 2

The bond-slip response associated with this model is shown in Fig. 8. It consists of two distinct branches: a first ascending non-linear branch (hyperbolic) reaching maximum stress τ_1 at the corresponding slip s_1, and a second descending branch (exponential), with a horizontal asymptote tending to zero. The parameter λ governs the curvature of the descending branch. This bond stress–slip model is expressed by Eq. (2) and is governed by three parameters: τ_1, s_1, λ [39]:

$$\tau(s) = \begin{cases} \tau_1 \sqrt{\dfrac{s}{s_1}}, & 0 \le s \le s_1 \\ \tau_1 e^{-\lambda\left(\frac{s}{s_1} - 1\right)}, & s > s_1 \end{cases} . \quad (2)$$

Table 3 Proposed model parameters

Material	d_b [mm]	s_1	τ_1	r	λ	R^2
Steel	10	0.19	22.58	1.20	0.24	0.978
	12	0.16	21.28	1.20	0.23	0.944
	14	0.14	19.41	1.22	0.22	0.917
AFRP	10	0.19	22.84	1.20	0.20	0.981
	12	0.16	21.63	1.20	0.20	0.982
	14	0.14	19.56	1.20	0.21	0.961
CFRP	10	0.19	21.63	1.20	0.25	0.947
	12	0.16	20.42	1.20	0.22	0.904
	14	0.14	18.72	1.20	0.28	0.958
GFRP	10	0.31	23.30	1.15	0.26	0.996
	12	0.18	21.06	1.20	0.20	0.944
	14	0.17	19.14	1.20	0.23	0.985

Fig. 9 displays a comparison of the simulation-generated results with models 1 and 2. By comparing the present results for the 10 mm steel bar with model 1, it is observed that the ascending branches converge, but the descending branch does not match. However, when compared with model 2, the situation is reversed: the first

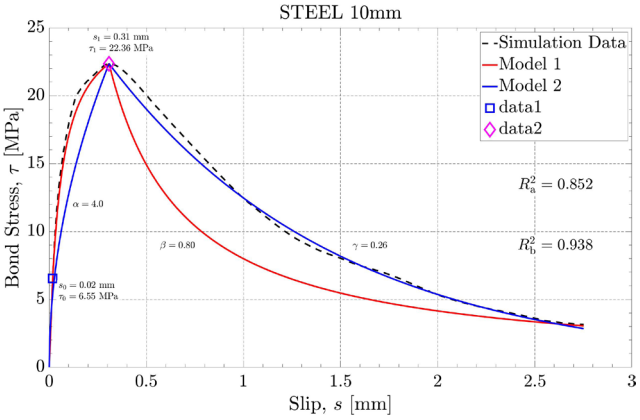

Fig. 9 Comparison of the bond stress-slip curves obtained from simulation results with models 1 and 2

ascending branch does not match, but the second descending branch aligns very well. In light of these results, we have proposed a model inspired by both models, consisting of a modified ascending branch from model 1 and the unchanged descending branch from model 2.

3.3 Bond-slip curve proposed model

As shown in the Fig. 10 the proposed model is constituted with two branches. An ascending curve from model 1, consisting of a linear branch followed by a second hyperbolic ascending branch, has been replaced by a single simple hyperbolic curve, as expressed in Eq. (3). This new ascending branch depends on three parameters: s_1, τ_1, and the parameter r, which governs the curvature of the ascending branch in the proposed model. It is easier to determine compared to the parameter α in model 1, which is often highly variable [38]. For the second descending branch of the proposed model, it remains the same as that of model 2, an exponential descending branch with a horizontal asymptote approaching 0. This is expressed by Eq. (3) as well, and is governed by three parameters: τ_1, s_1, and λ [39]:

$$\tau(s)=\begin{cases}\tau_1\times\dfrac{rs}{(r-1)s_1+s} & \text{for } s\le s_1\\ \tau_1\times e^{-\lambda\left(\frac{s}{s_1}-1\right)} & \text{for } s>s_1\end{cases}. \tag{3}$$

Thus, the proposed model, expressed by the bond stress–slip relationship in Eq. (3), is governed by four parameters: τ_1, s_1, r, and λ.

In order to assess the ability of this model to capture the overall bond behavior between the reinforcement and the concrete, it is necessary, in our case, to identify the model parameters from the numerical data recorded during the pull-out test simulation (Table 3).

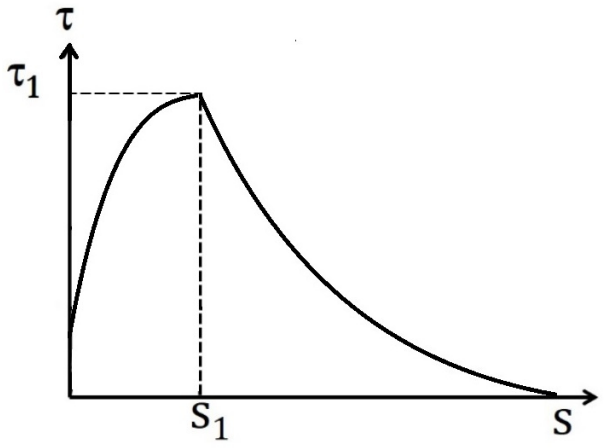

Fig. 10 The Bond-slip curve proposed model

According to Fig. 11, the prediction model fits remarkably well with the numerical results for all materials (Steel, AFRP, CFRP, GFRP) for the different bar diameters studied (10, 12, and 14 mm). This is evidenced by the predicted curves closely matching the simulations, with determination coefficients R^2 ranging from 0.904 to 0.996, with no significant divergence in either ascending or descending branches. Averaging the twelve cases examined, the shape parameter r is approximately 1.20, and the decay coefficient λ is close to 0.23. These values are retained as fixed representative parameters in our model for the various material and diameter configurations considered ($r = 1.20$, $\lambda = 0.23$).

3.4 Ultimate bond stress validation

The bond strength (τ_1) between concrete and reinforcement has been a topic of research for many years. Numerous researchers have studied the relationship between the pull-out load and the compressive strength of concrete f_c'. All studies in this field confirm the importance of compressive strength as a key factor influencing bond strength [5, 30].

Among these models, Huang et al. [40] proposed the following relation Eq. (4) for the ultimate bond stress:

$$\tau_1 = 0.45\times f_c'. \tag{4}$$

Tang and Cheng [23] proposed a formula Eq. (5) depending only on the concrete compressive strength:

$$\tau_1 = 8.9824\times e^{0.0193 f_c'}. \tag{5}$$

Other models take into account the variation in bar diameter as a secondary parameter in predicting the maximum bond stress.

Among these, Soroushian and Choi [41] developed the following empirical formula Eq. (6), based on partial pull-out tests of ribbed bars. This approach is consistent with the conditions of our simulation, in which the applied pull-out displacement is limited.

The corresponding formulation for this model [41] is presented in Eq. (6):

$$\tau_1 = \left(20-\frac{d_b}{4}\right)\sqrt{\frac{f_c'}{30}}. \tag{6}$$

Additionally, researchers have examined the impact of other variables such as the concrete cover thickness C_b, the reinforcement diameter d_b, the embedment length l_e, and the degree of concrete confinement provided by transverse reinforcement on bond strength [24, 35]. Recent studies have also investigated the effects of bar material

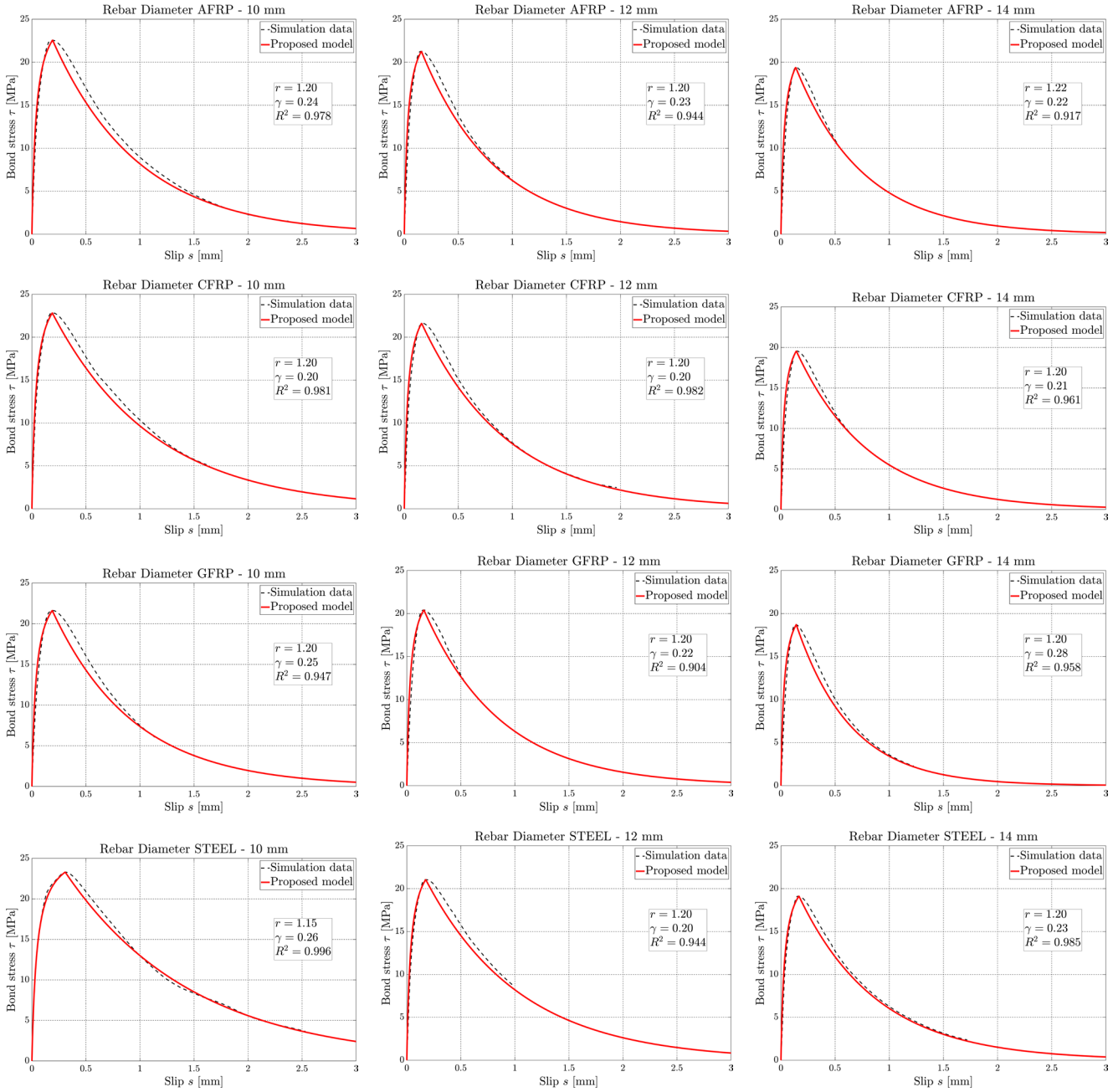

Fig. 11 Validation of proposed bond-slip model against numerical simulations for different bar types (STEEL, AFRP, CFRP, GFRP) and diameters (10 mm, 12 mm, 14 mm)

and geometry. Based on these studies, we selected certain prediction models [24, 42] that align with the conditions of our simulation, presented subsequently.

ACI Committee 440 [24] model provides an estimate of the bond strength between FRP bars and concrete. A linear regression of the normalized average bond stress is expressed as a function of the normalized concrete cover C_b/d_b and the embedment length d_b/l_d, derived from several practical tests. The choice of this code of practice over other existing codes is justified by the proximity of the estimated bond stress to actual test results [43].

The ultimate bond, according to ACI Committee 440 [24] is expressed by Eq. (7):

$$\tau_1 = 0.083\sqrt{f_c'}\left(4 + 0.3\frac{C_b}{d_b} + 100\frac{d_b}{l_d}\right). \tag{7}$$

Dong et al. [42] model improves upon ACI Committee 440 [24] by also incorporating the influence of rib geometry, including rib height h_r, width w_f, spacing s_r, and concrete rib width w_c, similar to our model. This model provides an estimation even closer to the results of actual tests [42], expressed by Eq. (8):

$$\tau_1 = f_c'^{0.472}\left(0.243 + 0.01\frac{d_b}{l_d} + 0.018\frac{w_c}{s_r d_b} + 0.021\frac{h_r}{d_b} + 9.554\frac{w_f}{s_r}\right). \quad (8)$$

To compare the maximum bond stress from simulations with prediction models, as detailed in Fig. 12, we start by analyzing the average value $\bar{\tau}_{\text{simulation}} = 20.96$ MPa against fixed prediction laws [34, 40], independent of the bar diameter: Tang and Cheng [23] predict $\tau_1 = 19.82$ MPa, which is a good estimate compared to the simulation (moderate difference of –1.14 MPa relative to the simulation), while Huang et al. [40] predict $\tau_1 = 18.45$ MPa, a more or less good estimate (difference of –2.51 MPa). Thus, we propose for the average maximum stress a relation close to that of Huang et al. [40], about half of the concrete strength, expressed by Eq. (9):

$$\bar{\tau} = 0.5 \times f_c'. \quad (9)$$

However, in the case of variable models where τ_1 depends on the bar diameter, it is more appropriate to compare the average bond stress for each diameter ($\bar{\tau}_{10\text{mm}} = 22.59$ MPa, $\bar{\tau}_{12\text{mm}} = 22.26$ MPa, $\bar{\tau}_{14\text{mm}} = 19.31$ MPa) individually with its corresponding predicted value for each model. First, the model proposed by Soroushian and Choi [41] slightly underestimates the bond stress across all diameters, with value $\tau_1 = 20.49$ MPa at ∅10 mm (deviation of –2.13 MPa), $\tau_1 = 19.87$ MPa at ∅12 mm (–1.09 MPa), and $\tau_1 = 20.94$ MPa at ∅14 mm (–0.02 MPa), demonstrating accuracy of our simulation result with this model.

The ACI Committee 440 [24] model underestimates the bond stress for smaller diameters ($\tau_1 = 15.71$ MPa at ∅10 mm, deviation of –6.88 MPa), this difference decreases at ∅12 mm ($\tau_1 = 18.32$ MPa, deviation of –2.94 MPa), and slightly overestimates it at ∅14 mm ($\tau_1 = 20.94$ MPa, deviation of +1.63 MPa). This marked underestimation for small diameters is consistent with the known conservative tendency of the ACI Committee 440 [24] model compared to experimental tests, as observed in the literature [42, 43].

On the other hand, the model in [42] proves closer to the simulation results, especially at ∅10 mm ($\tau_1 = 22.26$ MPa, deviation −0.33 MPa). It slightly overestimates (+0.97 MPa) for ∅12 mm and more noticeably at ∅14 mm (+2.90 MPa), but overall remains the closest to the simulation results with the model [42]. Since this model [42] is also closer to experimentally measured values compared to [24], which tends to underestimate them [42, 43], it can be concluded that the simulation results are likely closer to experimental outcomes.

4 Parametric analysis and generalized model

Since the current focuses on evaluating the bond performance of FRP bars compared to steel bars using a numerical simulation of the pull-out test, it is essential to observe the differences in maximum bond stress τ_1 and the

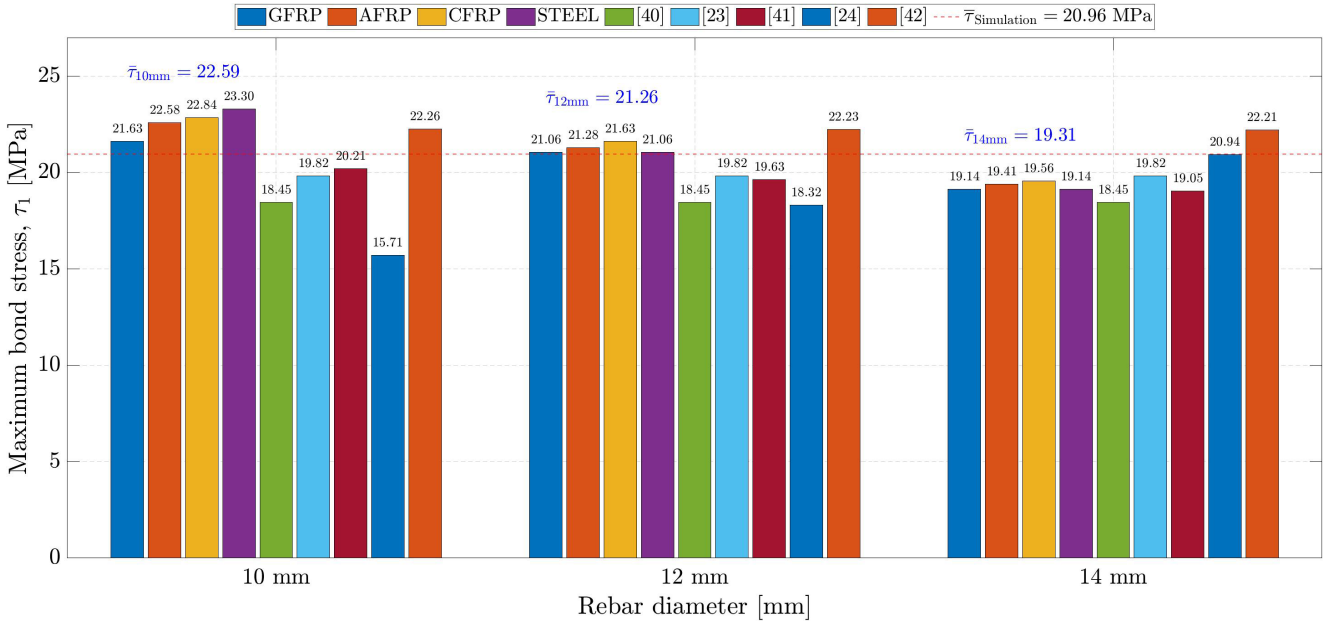

Fig. 12 Comparison of the maximum bond stress values from the simulation results and the predicted models

corresponding critical slip s_1 based on the variation in bar material for the studied diameters.

4.1 Effect of bar material variation

As shown in Fig. 13, it is observed that the maximum bond stress follows the same pattern depending on the bar material for all three diameters studied. The results show that CFRP bars exhibit the highest average bond stress (21.34 MPa), followed by AFRP (21.09 MPa), steel (21.01 MPa), and GFRP (20.60 MPa).

The only exception is for the 10 mm diameter, where steel bars show the highest bond stress. This behavior can be explained by the fact that, in steel bars with a diameter of 10 mm, the entire cross-section reaches the plastic zone at the same time that the surrounding concrete enters the strain-hardening phase under stress. During the plastic phase, the stress in the steel increases slowly, while deformation rises rapidly. This characteristic allows for additional hardening of the concrete, thereby delaying its damage. As a result, both the maximum stress and the corresponding slip increase, as observed in Fig. 14 for this particular specimen. However, in steel bars with diameters of 12 mm and 14 mm, only the contact zones near the ribs may reach the plastic state, while the rest of the steel bar remains in the elastic range throughout the pull-out process. Therefore, their behavior is similar to that of FRP bars, which exhibit purely elastic behavior.

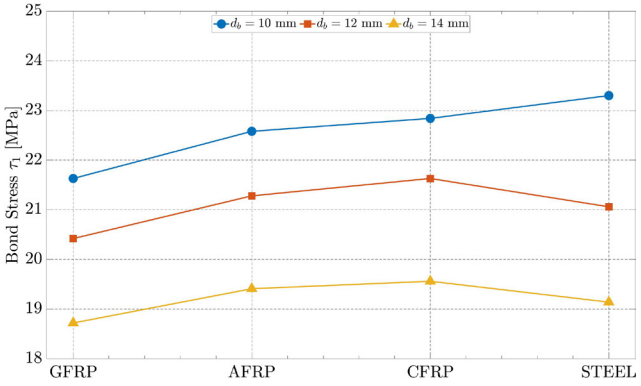

Fig. 13 Effect of bar material variation on the maximum bond stress

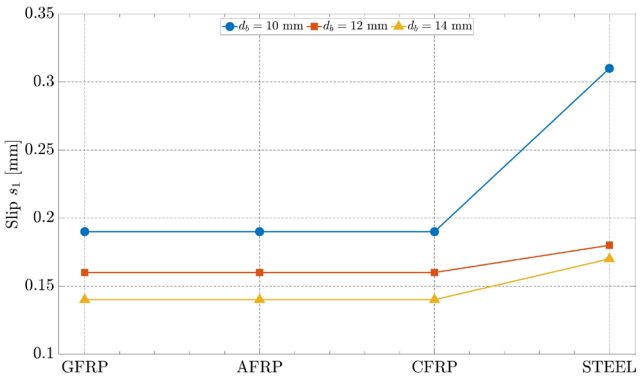

Fig. 14 Effect of bar material variation on the critical slip

Regarding the influence of bar material variation on the critical slip corresponding to the maximum bond stress, it appears to be governed by the mechanical behavior of the materials. As shown in Fig. 14, the slip does not vary with the type of material for all FRP bars.

This is due to their common linear elastic behavior. In contrast, the slip values for steel bars are slightly higher compared to FRP bars particularly for the bar with the smallest diameter. As previously explained, this is attributed to the plastic behavior of steel, which leads to greater deformation and, consequently, a larger slip value.

4.2 Effect of bar diameter variation

Fig. 15 shows the variation of maximum bond stress as a function of bar diameter for different materials. It is observed that the maximum bond stress (τ_1) decreases as the reinforcement diameter (d_b) increases, which is consistent with models reported in the literature [41, 42]. Therefore, an interpolation function of the simulation data with excellent correlation ($R^2 \approx 1$) was adopted for each material, similar to these models [42, 23], to serve as a predictive law for the maximum bond stress (τ_1), expressed in the general form given by Eq. (10):

$$\tau_1 = \bar{\tau}\left(a_{1_{MAT}} + \frac{a_{2_{MAT}}}{d_b} + a_{3_{MAT}} \times d_b\right), \tag{10}$$

where $\bar{\tau}$ is the mean maximum stress extracted from simulation results and depends directly on the contact nature (notably the friction coefficient) and the biaxial compressive strength f_c' according to Eq. (9), governed by both its uniaxial ultimate strength f_c and the confinement effect. In the simulation, for unconfined concrete, $f_c \approx f_c' = 41$ MPa [22].

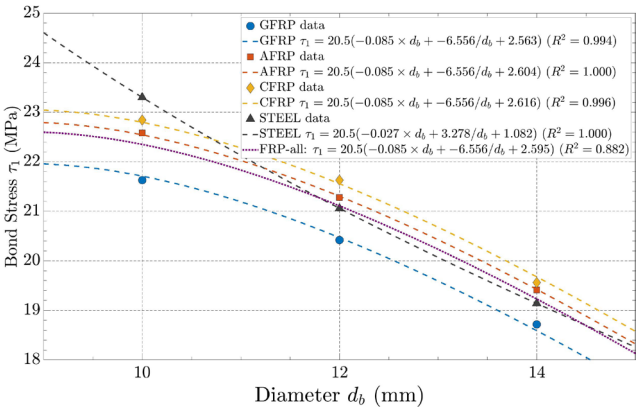

Fig. 15 Effect of bar material variation on the maximum bond stress

The other parameters $a_{1_{MAT}}$, $a_{2_{MAT}}$, and $a_{3_{MAT}}$ are related to the contact nature and material type (AFRP, CFRP, GFRP, and Steel), where the subscript *MAT* indicates the material type. These parameters are primarily linked to the mechanical behavior of the bars. As seen in Fig. 15, Steel displays a distinctly different shape due to its elasto-plastic bilinear behavior. In contrast, FRP bars exhibit the same non-linear trend with parallel curves and the same parameters of curvature $a_{2_{MAT}}$ and $a_{3_{MAT}}$, reflecting their shared elastic mechanical behavior. Based on the above, we can adopt a unified prediction model using the same formula for all FRP materials, which also demonstrates good predictive accuracy for steel bars with diameters of 12 mm and 14 mm that generally exhibit elastic behavior. Consequently, in cases involving lower-strength concrete that does not induce plastic deformation in the reinforcing steel bars, the same predictive function for the maximum bond stress can be applied to all reinforcement materials.

Concerning Fig. 16, which illustrates the variation of the critical slip s_1, corresponding to the maximum bond stress, as a function of diameter d_b for different materials, it is generally observed that the slip decreases with increasing diameter. However, a clear distinction can be made between steel and all FRP bars. In contrast, all FRP bars exhibit a similar and consistent behavior. This variation is strongly influenced by the mechanical properties of the materials. The homogeneous response observed among all FRP bars can be attributed to their shared purely linear elastic behavior, which results in a regular decrease in slip with increasing diameter, following a simple inverse power law expressed by Eq. (11):

$$s_1 = a_4 / d_b^{a_5} , \tag{11}$$

where a_4 and a_5 are fitting coefficients. For FRP bars, it is observed that $a_5 \approx 1$, indicating an almost inversely proportional relationship between slip and diameter. The strictly elastic and predictable behavior of FRP materials allows for a nearly perfect interpolation ($R^2 \approx 1$).

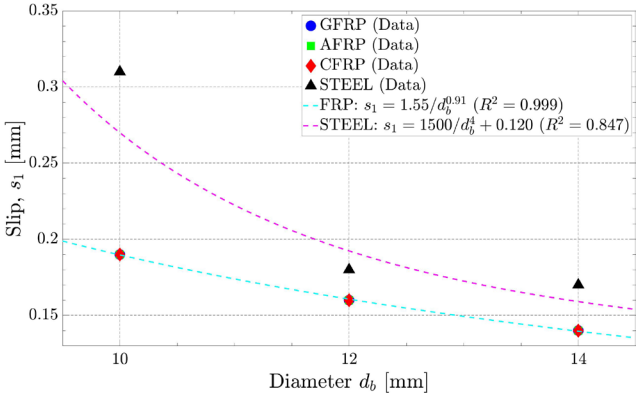

Fig. 16 Effect of bar material variation on the critical slip

For steel bars, characterized by a bilinear elasto-plastic behavior, the slip is governed by two mechanical regimes: the elastic phase followed by the plastic phase, which increases the slip compared to FRP bars. This behavior is modeled by a more complex interpolation function, as shown in Eq. (12) with a good correlation ($R^2 \approx 0.847$):

$$s_1 = a_4 / d_b^{a_5} + a_6 . \tag{12}$$

The new term a_6 represents the minimum limiting value of slip for large diameters, and the ratio $a_4/d_b^{a_5}$ with large coefficient values ($a_4 = 1500$ and $a_5 = 4$), reflects the sharp increase in slip for small diameters that exhibit plastic behavior. This results in significant elongation due to ductility, which considerably increases the slip. In cases where plastic behavior is entirely absent in steel, such as when using lower-strength concrete, the slip model should reduce to the same form as that used for FRP.

For simplicity, the same formula Eq. (12) can be adopted for all bars as a predictive law for the critical slip s_1, by setting $a_6 = 0$ for FRP.

4.3 Parametrized predictive bond–slip model

By substituting the prediction formula for the maximum bond stress Eq. (10) and Eq. (11) and the prediction formula for the critical slip Eq. (12) into our model equation (Eq. (3)), we obtain the final expression Eq. (13), with all its parameters summarized in Table 4:

$$\tau(s) = \begin{cases} 0.5 f_c' \left(a_{1_{MAT}} + \dfrac{a_{2_{MAT}}}{d_b} + a_{3_{MAT}} \times d_b \right) \times \dfrac{1.2\, s}{0.2\left(a_4 / d_b^{a_5} + a_6 \right) + s}, & s \le s_1 \\ 0.5 f_c' \left(a_{1_{MAT}} + \dfrac{a_{2_{MAT}}}{d_b} + a_{3_{MAT}} \times d_b \right) \times e^{-0.23\left(\frac{s}{\left(a_4 / d_b^{a_5} + a_6 \right)} - 1 \right)}, & s > s_1 \end{cases} . \tag{13}$$

Table 4 Parameters of the proposed predictive bond-slip model

Material bar	$a_{1_{MAT}}$	$a_{2_{MAT}}$	$a_{3_{MAT}}$	a_4	a_5	a_6
GFRP	2.563	−6.556	−0.085	1.55	0.91	0
AFRP	2.604					
CFRP	2.616					
All-FRP	2.595					
STEEL	1.082	+3.278	−0.027	1500	4.00	0.120

The comparison in Table 5 shows strong agreement between the simulation and the predictive model across all tests. The maximum bond stress (τ_1) exhibits a very low error (generally below 0.6%), while the critical slip (s_1) shows a minor error under 3% for FRP bars, and slightly higher deviations for steel bars: up to 12.4% for the 10 mm diameter, then decreasing to 9.8% and 4.3% for the larger 12 mm and 14 mm diameters, respectively, which corresponds to their degree of plastic deformation.

This variation in accuracy primarily stems from the higher regression quality obtained for FRP bars ($R^2 \approx 1$), reflecting their uniform linear elastic response, whereas the lower correlation for steel bars ($R^2 \approx 0.847$), associated with their bilinear elastoplastic behavior, leads to comparatively greater prediction deviations.

Graphical results in Fig. 17 confirm this strong trend agreement, with model and simulation curves nearly overlapping in the ascending and peak regions, supported by high R^2 values: ranging from 0.911 to 0.983 for FRP bars and 0.957 to 0.986 for Steel. The FRP-ALL model also provides an accurate average representation for FRP bars, with R^2 correlations ranging from 0.902 to 0.981.

Table 5 Comparison between simulation and proposed model predictions

d_b	Material	τ_1^{Sim}	τ_1^{Pred}	Err.%	s_1^{Sim}	s_1^{Pred}	Err.%
10 mm	GFRP	21.63	21.71	0.34	0.188	0.191	1.216
	AFRP	22.58	22.54	0.16	0.191	0.191	0.266
	CFRP	22.84	22.79	0.20	0.189	0.191	1.109
	STEEL	23.30	23.37	0.29	0.308	0.270	12.395
12 mm	GFRP	20.42	20.46	0.21	0.158	0.162	2.434
	AFRP	21.28	21.30	0.11	0.158	0.162	2.175
	CFRP	21.63	21.55	0.37	0.160	0.162	0.773
	STEEL	21.06	21.14	0.37	0.175	0.192	9.845
14 mm	GFRP	18.72	18.58	0.71	0.142	0.140	0.780
	AFRP	19.41	19.42	0.04	0.136	0.140	2.930
	CFRP	19.56	19.67	0.59	0.142	0.140	1.199
	STEEL	19.14	19.23	0.50	0.166	0.159	4.304

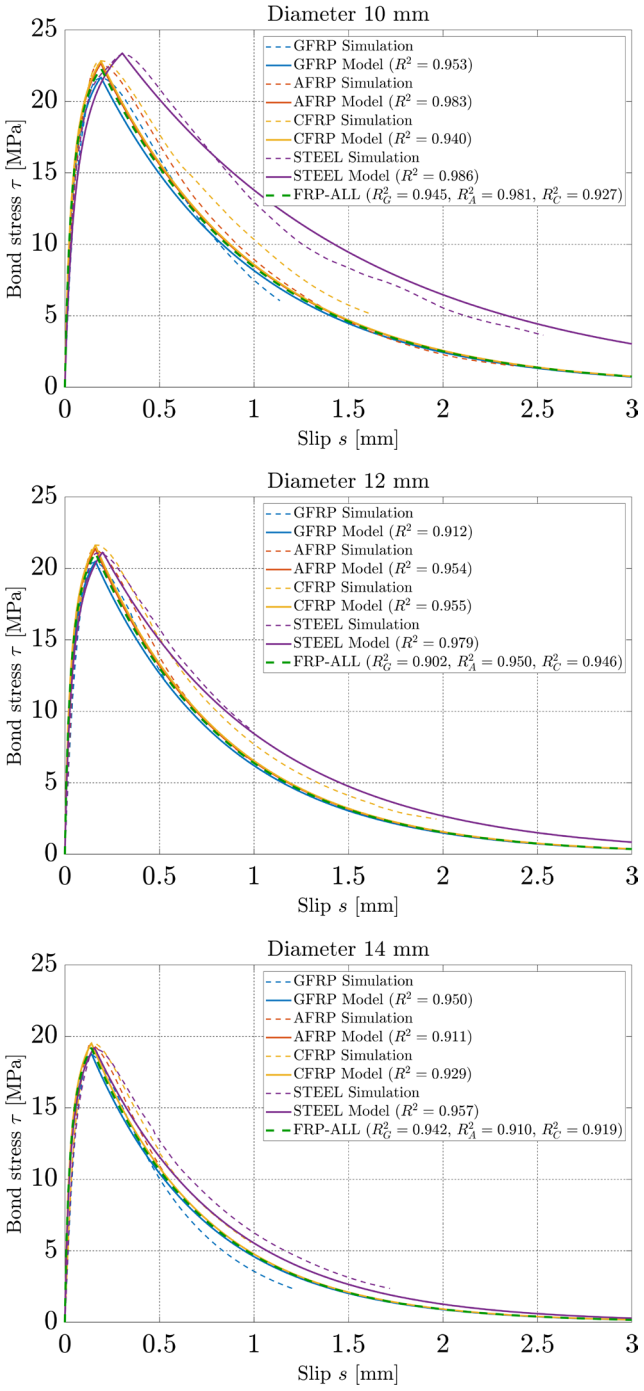

Fig. 17 Comparison of bond–slip curves between predictions from the proposed model and numerical simulation results for different bar types (GFRP, AFRP, CFRP, steel) and diameters (10 mm, 12 mm, 14 mm)

5 Conclusions

The current study focuses on the evaluation of the bond performance between concrete and reinforcement bars carried out via numerical simulation of a pull-out test. Different FRP rebar types (GFRP, AFRP and CFRP) were

employed alongside Steel reinforcement, and three diameters — 10 mm, 12 mm, and 14 mm — were considered in the simulations.

An unconfined concrete using a regularized Drucker–Prager microplane model was proposed. This concrete model was integrated into the pull-out test simulation with a Mohr–Coulomb contact law incorporating material-specific friction coefficients for each bar material. The model also included elasto-plastic behavior for steel and linear elastic law for FRP bars. Validation of the simulated bond–slip curves was performed by comparing the obtained results with two reference analytical models. The main findings of this study can be summarized as follows:

- All the bond–slip curves obtained from the simulations accurately match the analytical models, reproducing the typical shape of the bond stress–slip relationship.
- A modified hybrid model was proposed, showing excellent agreement with the simulation results, with correlation coefficients (R^2) ranging from 0.904 to 0.996.
- The type of reinforcement material has a noticeable impact on the maximum bond stress. CFRP bars show the highest average bond stress, followed by AFRP, steel, and GFRP. However, an exception was noted for the ∅10 mm steel bar, as its plastic deformation led to the highest bond stress among all tested configurations.
- The maximum bond stress (τ_1) decreases as the diameter (d_b) of the reinforcement increases for all types of rebars.
- The type of reinforcement also affects the critical slip (s_1), which remains relatively uniform for FRP bars due to their similar linear elastic behavior, while it is higher and variable for steel due to the effects of plasticity.
- The critical slip (s_1) generally decreases with increasing bar diameter, especially for FRP bars, where the reduction is progressive and consistent. In contrast, steel bars show less predictable variation due to plasticity effects.
- A complete parameterized predictive model was developed to characterize the bond–stress behavior as a function of bar diameter and concrete compressive strength, utilizing material-specific coefficients. The model demonstrates excellent agreement with simulation results, achieving maximum bond stress prediction errors below 0.6%, critical slip deviations within 3% for FRP bars, and variable but quantifiable deviations for steel (ranging from 4% to 12% depending on plastic deformation effects). Strong curve correlations were observed, with coefficients of determination (R^2) ranging from 0.911 to 0.983 across all configurations.

An important distinction emerges from the analysis of the results when comparing the behavior of steel and FRP reinforcements, even though their bond performance appears nearly equivalent. Steel exhibits superior adaptability thanks to its ductile behavior and the presence of a plastic phase; however, this same characteristic introduces complexity in achieving accurate predictive modeling. Conversely, FRP bars display a consistent linear-elastic response up to rupture, despite their inherent brittleness. This linearity not only simplifies numerical prediction but, when coupled with the programmable integration of their mechanical properties and surface characteristics during manufacturing, also makes it possible to design customized and more advanced FRP bars tailored to specific structural demands. Such an approach could significantly reduce dependence on destructive physical testing after production.

Finally, to optimize the proposed numerical model, future works should first focus on completing a parametric analysis by investigating, through extended simulations, the influence of key parameters such as bar stiffness, concrete confinement degree, variations in friction coefficients, reinforcement rib geometry, concrete cover thickness, and anchorage length. This approach will enable the development of a more advanced and generalized prediction model that can significantly reduce the need for extensive experimental campaigns. Subsequently, targeted validation through a limited number of pull-out experimental tests on representative specimens will be sufficient to confirm the enhanced model's accuracy and its ability to realistically represent in-service structural conditions. Lastly, extending the simulation framework to cyclic and dynamic loading scenarios would further broaden its applicability to seismic and fatigue-related performance assessments.

References

[1] International Federation for Structural Concrete (fib) "FRP Reinforcement in RC Structures", International Federation for Structural Concrete (fib), Lausanne, Switzerland, Rep. fib Bulletin No. 40, 2007. ISBN 978-2-88394-080-2 https://doi.org/10.35789/fib.BULL.0040

[2] Coccia, S., Imperatore, S., Rinaldi, Z. "Influence of corrosion on the bond strength of steel rebars in concrete", Materials and Structures, 49(1), pp. 537–551, 2016. https://doi.org/10.1617/s11527-014-0518-x

[3] ACI Committee 440 "State-of-the-Art Report on Fiber Reinforced Plastic (FRP) Reinforcement for Concrete Structures", American Concrete Institute, Farmington Hills, MI, USA, Rep. ACI 440R-96 (Reapproved 2002), 1996.

[4] Sólyom, S., Di Benedetti, M., Balázs, G. L. "Effect of Surface Characteristics of FRP Bars on Bond Behavior in Concrete", In: The 13th International Symposium on Fiber-Reinforced Polymer Reinforcement for Concrete Structures, Anaheim, CA, USA, 2017, SP-327—41. ISBN 978-1-64195-046-6 [online] Available at: https://www.researchgate.net/publication/333670843

[5] Zhao, W., Zhu, B. "Basic parameters test and 3D modeling of bond between high-strength concrete and ribbed steel bar after elevated temperatures", Structural Concrete, 18(5), pp. 653–667, 2017. https://doi.org/10.1002/suco.201600005

[6] Achillides, Z., Pilakoutas, K. "FE modelling of bond interaction of FRP bars to concrete", Structural Concrete, 7(1), pp. 7–16, 2006. https://doi.org/10.1680/stco.2006.7.1.7

[7] ANSYS, Inc. "ANSYS Mechanical APDL Element Reference", [pdf] Release 14.0, Canonsburg, PA, USA, 2011. Available at: https://www.mm.bme.hu/~gyebro/files/vem/ansys_14_element_reference.pdf

[8] ANSYS, Inc. "ANSYS Contact Technology Guide", Release 9.0, ANSYS, Inc., Canonsburg, PA, USA, 2004. [online] Available at: https://www.academia.edu/40430543/ANSYS_Contact_Technology_Guide

[9] Ibrahim, A. M. A., Fahmy, M. F. M., Wu, Z. "Numerical simulation on fracturing bond mechanisms of different basalt FRP bars", Journal of Japan Society of Civil Engineers, Ser. A2 (Applied Mechanics (AM)), 71(2), pp. I_289–I_298, 2015. https://doi.org/10.2208/jscejam.71.I_289

[10] Orlando, N., Benvenuti, E. "Advanced XFEM simulation of pull-out and debonding of steel bars and FRP-reinforcements in concrete beams", American Journal of Engineering and Applied Sciences, 9(3), pp. 746–754, 2016. https://doi.org/10.3844/ajeassp.2016.746.754

[11] Fava, G., Carvelli, V., Pisani, M. A. "Remarks on bond of GFRP rebars and concrete", Composites Part B: Engineering, 93, pp. 210–220, 2016. https://doi.org/10.1016/j.compositesb.2016.03.012

[12] Zanuy, C., Curbach, M., Lindorf, A. "Finite element study of bond strength between concrete and reinforcement under uneven confinement condition", Structural Concrete, 14(3), pp. 260–270, 2013. https://doi.org/10.1002/suco.201200019

[13] Tabatabaei Mirhosseini, R., Araghizadeh, E., Rashidi, S. "Approximate relationship for the bond-slip using a concrete damage-plastic model", Advances in Materials Science and Engineering, 2023, 1320192, 2023. https://doi.org/10.1155/2023/1320192

[14] Wei-ping, Z. "Local Bond-slip Numerical Simulation Based on ANSYS Contact Analysis", In: 2011 International Conference on Electric Technology and Civil Engineering (ICETCE), Lushan, China, 2011, pp. 438–441. ISBN 978-1-4577-0289-1 https://doi.org/10.1109/ICETCE.2011.5775869

[15] Eddy, L., Matsumoto, K., Nagai, K., Wang, Z. "Investigation of effect of local bond model on crack propagation in RC using 3D RBSM", In: Computational Modelling of Concrete Structures, CRC Press, 2018, pp. 755–766. ISBN 978-1-138-74117-1 https://doi.org/10.1201/9781315182964-89

[16] García Sánchez, J. A., Quintero Ramírez, C., Gonçalves, P. C., Javier Begambre, O. "Bond behavior of auxetic bars in reinforced concrete – A numerical study", Latin American Journal of Solids and Structures, 21(3), e538, 2024. https://doi.org/10.1590/1679-78257917

[17] Jin, L., Liu, M., Zhang, R., Du, X. "3D meso-scale modelling of the interface behavior between ribbed steel bar and concrete", Engineering Fracture Mechanics, 239, 107291, 2020. https://doi.org/10.1016/j.engfracmech.2020.107291

[18] Jiang, T., Wu, Z., Huang, L., Ye, H. "Three-dimensional nonlinear finite element modeling for bond performance of ribbed steel bars in concrete under lateral tensions", International Journal of Civil Engineering, 18(5), pp. 595–617, 2020. https://doi.org/10.1007/s40999-019-00488-1

[19] Panteki, E., Máca, P., Häussler-Combe, U. "Finite element analysis of dynamic concrete-to-rebar bond experiments in the push-in configuration", International Journal of Impact Engineering, 106, pp. 155–170, 2017. https://doi.org/10.1016/j.ijimpeng.2017.03.016

[20] Quayyum, S. "Bond behaviour of fibre reinforced polymer (FRP) rebars in concrete", MSc Thesis, University of British Columbia, Kelowna, BC, Canada, 2010. [online] Available at: https://www.researchgate.net/publication/277868457

[21] Assaad, F., Hany, N., Fawaz, G., Hantouche, E., Harajli, M. "Effect of active and passive concrete confinement on the bond stress-slip response of steel bars in tension", Construction and Building Materials, 305, 124737, 2021. https://doi.org/10.1016/j.conbuildmat.2021.124737

[22] Mander, J. B., Priestley, M. J. N., Park, R. "Theoretical stress-strain model for confined concrete", Journal of Structural Engineering, 114(8), pp. 1804–1826, 1988. https://doi.org/10.1061/(ASCE)0733-9445(1988)114:8(1804)

[23] Tang, C.-W., Cheng, C.-K. "Modeling local bond stress–slip relationships of reinforcing bars embedded in concrete with different strengths", Materials, 13(17), 3701, 2020. https://doi.org/10.3390/ma13173701

[24] ACI Committee 440 "Guide for the design and construction of structural concrete reinforced with fiber-reinforced polymer (FRP) bars", American Concrete Institute, Farmington Hills, MI, USA, Rep. ACI 440.1R-15, 2015.

[25] Chiriatti, L., Mercado-Mendoza, H., Apedo, K. L., Fond, C., Feugeas, F. "A study of bond between steel rebar and concrete under a friction-based approach", Cement and Concrete Research, 120, pp. 132–141, 2019. https://doi.org/10.1016/j.cemconres.2019.03.019

[26] Comité Euro-International du Béton (CEB) "CEB-FIP Model Code 1990: Design Code", Thomas Telford Servies Ltd., 1993. ISBN 9780727735430

[27] Centre Scientifique et Technique du Bâtiment (CSTB) "Règles techniques de conception et de calcul des ouvrages et constructions en béton armé suivant la méthode des états limites" (Technical rules for the design and calculation of reinforced concrete structures according to the limit state method), Règles BAEL 91 révisées 99 (DTU P 18-702), 2000. (in French)

[28] Raous, M., Ali Karray, M. "Modelling coupling friction and adhesion for steel–concrete interfaces", International Journal of Computational Applications in Technology, 34(1), pp. 42–51, 2009. https://doi.org/10.1504/IJCAT.2009.022701

[29] Karray, M. A., Barbarin, S., Raous, M. "Traitement de la liaison béton/acier par un modèle d'interface couplant adhésion et frottement" (Treatment of concrete/steel bond using an interface model coupling adhesion and friction), Annales Maghrébines de l'Ingénieur, hal-03177664, 2004. Available at: https://hal.science/hal-03177664 (in French)

[30] Zhao, W., Zhu, B. "Theoretical model for the bond–slip relationship between ribbed steel bars and confined concrete", Structural Concrete, 19(2), pp. 548–558, 2018. https://doi.org/10.1002/suco.201700008

[31] Yuan, J. S., Hadi, M. N. S. "Friction coefficient between FRP pultruded profiles and concrete", Materials and Structures, 51(5), 120, 2018. https://doi.org/10.1617/s11527-018-1250-8

[32] Shaia, H. A., Al-Asadi, A. K., Ramadan, S. H. "Evaluation of the interface friction between fiber-reinforced polymers and granular materials using modified shear apparatus", International Journal of Civil Engineering and Technology, 9(13), pp. 1017–1026, 2018. [online] Available at: https://iaeme.com/Home/article_id/IJCIET_09_13_102

[33] Sun, N., Song, Y., Hou, W., Zhang, H., Wu, D., Li, Y., Gong, Y. "Interfacial bond properties between normal strength concrete and epoxy resin concrete", Advances in Materials Science and Engineering, 2021, 5561097, 2021. https://doi.org/10.1155/2021/5561097

[34] Lin, H., Zhao, Y., Ozbolt, J., Feng, P., Jiang, C., Eligehausen, R. "Analytical model for the bond stress-slip relationship of deformed bars in normal strength concrete", Construction and Building Materials, 198, pp. 570–586, 2019. https://doi.org/10.1016/j.conbuildmat.2018.11.258

[35] Alhusban, M., Parvin, A. "Finite Element Analysis of Axially Loaded RC Walls with Openings Strengthened Using Textile Reinforced Mortar for Sustainable Structures", Buildings, 12(11), 1993, 2022. https://doi.org/10.3390/buildings12111993

[36] Németh, O. I., Lublóy, É., Farkas, G. "Bond of reinforcement in polymer concrete", Periodica Polytechnica Civil Engineering, 58(2), pp. 137–141, 2014. https://doi.org/10.3311/PPci.7502

[37] Akbarifar, R., Mortezaei, A., Babaei, A. "Meso-scale Study of Bond Behavior between Ribbed Steel Rebar and Fiber-reinforced Cementitious Composite Considering Rebar Rib Geometry", Periodica Polytechnica Civil Engineering, 68(4), pp. 1350–1366, 2024. https://doi.org/10.3311/PPci.28772

[38] Rolland, A., Argoul, P., Benzarti, K., Quiertant, M., Chataigner, S., Khadour, A. "Analytical and numerical modeling of the bond behavior between FRP reinforcing bars and concrete", Construction and Building Materials, 231, 117160, 2020. https://doi.org/10.1016/j.conbuildmat.2019.117160

[39] Lu, X. Z., Teng, J. G., Ye, L. P., Jiang, J. J. "Bond–slip models for FRP sheets/plates bonded to concrete", Engineering Structures, 27(6), pp. 920–937, 2005. https://doi.org/10.1016/j.engstruct.2005.01.014

[40] Huang, Z., Engström, B., Magnusson, J. "Experimental and analytical studies of the bond behavior of deformed bars in high strength concrete", In: Fourth International Symposium on Utilization of High Strength/High Performance Concrete, vol. 3, Paris, France, 1996, pp. 1115–1124.

[41] Soroushian, P., Choi, K.-B. "Local bond of deformed bars with different diameters in confined concrete", ACI Structural Journal, 86(2), pp. 217–222, 1989. https://doi.org/10.14359/2731

[42] Dong, H. L., Li, D. F., Yang, J. "Bond strength prediction model of ribbed FRP bars in concrete", Journal of Physics: Conference Series, 2476, 012018, 2023. https://doi.org/10.1088/1742-6596/2476/1/012018

[43] Yan, F., Lin, Z., Yang, M. "Bond mechanism and bond strength of GFRP bars to concrete: A review", Composites Part B: Engineering, 98, pp. 56–69, 2016. https://doi.org/10.1016/j.compositesb.2016.04.068